

RESEARCH LETTER

10.1002/2016GL072250

Key Points:

- Currently, Ceres obliquity is only 4° ; we have calculated Ceres obliquity history and found that it undergoes large periodic oscillations
- At higher obliquities, only few PSRs remain; we find a correlation between persistent PSRs and bright crater floor deposits
- Bright deposits in PSR craters are likely volatiles accumulated in cold traps: water molecules from the exosphere or exposed ground ice

Supporting Information:

- Data Set S1
- Data Set S2
- Data Set S3
- Text S1
- Figure S1
- Figure S2

Correspondence to:

A. I. Ermakov,
eai@caltech.edu

Citation:

Ermakov, A. I., E. Mazarico, S. E. Schröder, U. Carsenty, N. Schorghofer, F. Preusker, C. A. Raymond, C. T. Russell, and M. T. Zuber (2017), Ceres's obliquity history and its implications for the permanently shadowed regions, *Geophys. Res. Lett.*, *44*, doi:10.1002/2016GL072250.

Received 9 DEC 2016

Accepted 14 FEB 2017

Ceres's obliquity history and its implications for the permanently shadowed regions

A. I. Ermakov^{1,2}, E. Mazarico³, S. E. Schröder⁴, U. Carsenty⁴, N. Schorghofer⁵, F. Preusker⁴, C. A. Raymond², C. T. Russell⁶, and M. T. Zuber¹

¹Department of Earth, Atmospheric and Planetary Sciences, Massachusetts Institute of Technology, Cambridge, Massachusetts, USA, ²Jet Propulsion Laboratory, California Institute of Technology, Pasadena, California, USA, ³NASA Goddard Space Flight Center, Greenbelt, Maryland, USA, ⁴Institute of Planetary Research, German Aerospace Center, Berlin, Germany, ⁵Institute for Astronomy, University of Hawai'i at Mānoa, Honolulu, Hawaii, USA, ⁶IGPP/EPSS, University of California, Los Angeles, California, USA

Abstract Due to the small current obliquity of Ceres ($\epsilon \approx 4^\circ$), permanently shadowed regions (PSRs) exist on the dwarf planet's surface. Since the existence and persistence of the PSRs depend on the obliquity, we compute the obliquity history over the last 3 Myr and find that it undergoes large oscillations with a period of 24.5 kyr and a maximum of $\epsilon_{\max} \approx 19.6^\circ$. During periods of large obliquity, most of the present-day PSRs receive direct sunlight. Some craters in Ceres's polar regions possess bright crater floor deposits (BCFDs). We find an apparent correlation between BCFDs and the most persistent PSRs. In the north, only two PSRs remain at ϵ_{\max} and they both contain BCFDs. In the south, one of the two only craters that remain in shadow at ϵ_{\max} contains a BCFD. The location of BCFDs within persistent PSRs strongly suggests that BCFDs consist of volatiles accumulated in PSR cold traps: either water molecules trapped from the exosphere or exposed ground ice.

1. Introduction

1.1. What Did We Know Before Dawn?

The shape of dwarf planet (1) Ceres and orientation of its spin pole (and, therefore, obliquity) had been constrained in several studies prior to the Dawn mission [Thomas *et al.*, 2005; Drummond and Christou, 2008; Carry *et al.*, 2008; Drummond *et al.*, 2014]. The uncertainties of these determinations were typically on the order of 5° . Skoglöv *et al.* [1996] conducted a study of obliquity variations of 10 large asteroids including Ceres using the then available spin vectors and ellipsoidal shape models and concluded that orbital evolution characteristic frequencies are typically higher than precession frequencies. No indication of chaos in 2 Myr integrations was found. Bills and Nimmo [2011] predicted that Ceres has a tidally damped obliquity, which, if true, presents an additional constraint on the internal structure, as it would depend on the moments of inertia. However, Rambaux *et al.* [2011] argued that the damping period is on the order of 10^{17} years—much longer than the age of the solar system—and, therefore, it is highly unlikely that the present-day obliquity is damped. Hayne and Aharonson [2015] studied water ice stability on the surface of Ceres using statistical, artificial topography and concluded that ice becomes stable at latitudes higher than $\approx 60^\circ$ within persistent shadows on steep slopes and within permanently shadowed regions (PSRs).

1.2. Motivation

Images from the Dawn spacecraft's Framing Camera (FC) and radio tracking of the spacecraft from ground-based stations have allowed the precise determination of the Ceres's rotational pole [Park *et al.*, 2016] and, therefore, of the dwarf planet's obliquity (ϵ). Presently, Ceres's obliquity is about 4° [Russell *et al.*, 2016]. Due to this low obliquity, permanently shadowed regions have been detected on Ceres's surface using the Dawn Framing camera images and shape-based illumination modeling [Schorghofer *et al.*, 2016; Platz *et al.*, 2017]. This makes Ceres only the third body in the solar system after the Moon [Zuber and Smith, 1997; Mazarico *et al.*, 2011] and Mercury [Chabot *et al.*, 2012; Neumann *et al.*, 2013] with identified PSRs. The existence of PSRs depends critically on the body's obliquity.

Some craters in Ceres's polar regions possess bright crater floor deposits or BCFDs. These crater floors are typically in shadow, but they receive light scattered from the surrounding sunlit crater walls and therefore

can be seen by the FC. Temperatures inside PSRs can be so cold that the sublimation rate of surface water ice becomes negligible. Therefore, any ice delivered by an exosphere or exposed by impacts may remain indefinitely. We hypothesize that BCFDs are volatile deposits accumulated in PSR cold traps analogous to the Moon and Mercury [Watson *et al.*, 1961; Arnold, 1979; Slade *et al.*, 1992; Feldman *et al.*, 1998; Paige *et al.*, 2010; Sanin *et al.*, 2012; Moores, 2016]. The boundaries of Ceres's cold traps are determined by the PSRs at $\epsilon = \epsilon_{\max}$.

The analysis of the Gamma Ray and Neutron Detector (GRaND) data shows that Ceres's regolith is rich in hydrogen [Prettyman *et al.*, 2016]. Neutron and gamma ray count data reveal a strong latitude variation with suppressed counts at high latitudes. The lower bound of H concentration near the poles exceeds that found in carbonaceous chondrites, which are thought to be the best meteoritic analogues of Ceres. Therefore, the GRaND observations indicate that water ice and/or other volatile species may be concentrated in the polar regions on or very near (≈ 1 m) the surface. Nevertheless, water ice is rarely found exposed on the sunlit surface [Combe *et al.*, 2016].

The observation of BCFDs on Ceres is similar to the observations within Mercury's PSRs by the Mercury Surface, Space ENvironment, GEochemistry, and Ranging (MESSENGER) spacecraft. The MESSENGER images show regions with higher reflectance inside some PSRs, with the boundary of the higher-reflectance units closely matching the PSR boundaries [Neumann *et al.*, 2013; Chabot *et al.*, 2014; Deutsch *et al.*, 2016]. One important difference between the PSR inventory from the MESSENGER and Dawn data is that the heights of Mercury's topography were derived from laser altimetry [Cavanaugh *et al.*, 2007; Zuber *et al.*, 2012], which is independent of the illumination conditions, whereas Ceres's elevations are derived from stereo analysis of the FC images.

Orbital and obliquity histories have been shown to be important factors for volatile transport on the Moon, Mercury, and Mars. Siegler *et al.* [2013] concluded that due to Mercury's low obliquity, variations in orbital eccentricity are likely to have been the dominant cause of changes in polar temperatures on this planet. Siegler *et al.* [2015] found that cold traps are likely to have been stable for nearly 4 Gyr on Mercury. The Moon has undergone a major spin axis reorientation in the past [Ward, 1975]. Siegler *et al.* [2011] conclude that lunar obliquity history has dramatically altered the lunar polar thermal environment. In the following work, Siegler *et al.* [2015] found that when the Moon was at approximately half of its current semimajor axis (3 ± 1 Gyr), lunar obliquity may have reached as high as 77° . At that time, lunar polar temperatures were much higher and cold traps could not exist. Later, lunar obliquity has decreased creating environments favorable for water ice stability. More recently, Siegler *et al.* [2016] provided an example of a possible feedback between knowledge of volatile distribution and body orientation history. Additionally, it has been predicted that the obliquity forcing is one of the main drivers of the volatile transport on Mars [Jakosky and Phillips, 2001; Laskar *et al.*, 2004; Jakosky *et al.*, 2005].

Thus, in the case of Ceres, understanding temporal obliquity variations in the past sheds light on the history of PSRs and can help constrain the timescales for water ice deposition and loss and ultimately might constrain the amount of water delivered to Ceres from exogenic sources.

1.3. Outline

We start by describing the orbit and rotation integrator and the illumination model in section 2. We then summarize the available shape and orientation data as well as the observations of Ceres's BCFDs in section 3. The results on Ceres's obliquity, PSR history, and their relation to BCFDs are presented in section 4. We discuss the implications of our results in section 5 and summarize our findings in section 6.

2. Methods

2.1. Integrator

We used a symplectic integrator to backward integrate the orbital and rigid body motion of Ceres. The symplectic mapping for the N-planet problem was developed by Wisdom and Holman [1991]. It has been proven to be an efficient algorithm for long-term integrations of planetary systems. Later, similar ideas led to the development of a symplectic mapping for the rigid body dynamics [Touma and Wisdom, 1994]. We use a symplectic leapfrog algorithm, in which an accuracy of $\mathcal{O}(h^2)$ is achieved by shifting the phase of the Dirac delta functions by a half of the integration time step h . General leapfrog mapping can be written in the form

$$\mathcal{A}_K(h/2) \circ \mathcal{B}_N(h) \circ \mathcal{A}_K, \quad (1)$$

where, for the case of the N-planet problem, \mathcal{A}_K is the mapping according to the Keplerian Hamiltonian and \mathcal{B}_{NI} is the mapping according to the interactions Hamiltonian. The complete mapping for spin-orbit dynamics can be written as the rigid body leapfrog mapping nested into the N-planets leapfrog mapping as follows:

$$\mathcal{A}_K(h/2) \circ \mathcal{A}_2(h/4) \circ \mathcal{B}_3(h/2) \circ \mathcal{A}_2(h/4) \circ \mathcal{B}_{\text{NI}}(h) \circ \mathcal{B}_{\text{RI}}(h) \circ \mathcal{A}_K(h/2) \circ \mathcal{A}_2(h/4) \circ \mathcal{B}_3(h/2) \circ \mathcal{A}_2(h/4), \quad (2)$$

where \mathcal{A}_2 is the axisymmetric rigid body motion, \mathcal{B}_3 is the perturbation in the rigid body motion due to the body's triaxiality, \mathcal{B}_{RI} is the rotational interactions between Ceres and other bodies, i.e., the Sun and the planets. In our case, the spin-orbit coupling term acts in \mathcal{B}_{RI} . The choice of time step h is crucial for the accuracy of the mapping. We choose a value of 1/20 of the fastest periodic motion considered. We performed integrations both with biaxial and triaxial Ceres. For the case of triaxial Ceres, the shortest period is the rotational period (9.07 h). Therefore, for these integrations we set $h = 1620$ s. For the case of a biaxial Ceres, the shortest period is the orbital period of Mercury (≈ 88 days); accordingly, we can use $h = 4.4$ days. A detailed description of the integrator is available in the supporting information.

2.2. Illumination Modeling Using Digital Terrain Model

In order to assess the illumination conditions at Ceres over a range of past obliquities, we performed numerical illumination modeling using a shape model of Ceres. This approach has been used in the past for the Moon and Mercury, using a shape model derived from laser altimetry data [Mazarico *et al.*, 2011; Neumann *et al.*, 2013]. We follow the approach described in Schorghofer *et al.* [2016] using ray tracing over multilevel, multi-resolution triangulated meshes. The extended nature of the Sun as a light source is handled by discretizing its disc into 500 point sources. For the present-day orientation of Ceres, we use the current best estimates consistent with the adopted shape model [Preusker *et al.*, 2015, 2016]. While Schorghofer *et al.* [2016] resampled the High Altitude Mapping Orbit (HAMO)-derived Digital Terrain Model (DTM) onto a grid of points uniformly spaced in north polar stereographic projection, we took advantage of the full resolution of the DTM high-level products by implementing the Lambert-Azimuthal Equal Area projection [Snyder, 1982] and performing the simulations in that projection at a resolution of 135 m/pixel down to $\approx 53.5^\circ$ latitude. For computational reasons and because of Ceres's rapid spin (rotational period ≈ 9.07 h) and long orbital period (4.6 years), we restricted our simulations to a full rotation at each pole's respective solstice, which is the geometry that provides the strongest constraint regarding the presence of long-lived shadows.

3. Data

3.1. Ceres Shape

The shape model of Ceres was produced using a stereophotogrammetry (SPG) technique applied by the German Aerospace Center (DLR) [Preusker *et al.*, 2016]. The SPG method is purely geometrical and does not rely on simultaneously solving for surface heights and albedo. The global shape model used here was computed from images acquired during Dawn's HAMO phase (High Altitude Mapping Orbit: 6 weeks at ≈ 1500 km altitude), at a resolution of ≈ 135 m/pixel. Thanks to the high sensitivity of the Dawn's Framing Camera [Sierks *et al.*, 2011; Schröder *et al.*, 2013], it is possible to utilize features seen in scattered light to constrain the shape of the floors of shadowed polar craters, despite larger ray intersection errors and the need for interpolation near those locations. The comparison of the area in permanent shadow derived from numerical illumination simulations performed with a shape model [Schorghofer *et al.*, 2016] and that obtained from a survey of minimum shadows observed by FC near northern solstice [Platz *et al.*, 2017] shows an agreement to $\approx 2\%$, which brings confidence in the modeling methodology and DTM quality for illumination modeling. However, we find that the HAMO DTM resolution and accuracy are typically not sufficient to model the conditions within small craters (< 4 km). We also used the shape reconstructed for the southern hemisphere. Despite the unfavorable lighting conditions, as Dawn visited Ceres during southern winter, the HAMO DTM allows illumination modeling outside of the immediate polar region ($85^\circ - 90^\circ$ S), which was in seasonal darkness. Additionally, we conducted a sensitivity test by perturbing the crater depths by 100 m, which is a conservative estimate of the height error, and recomputing the PSR boundaries. We concluded that the DTM errors do not significantly affect our results in the larger craters.

3.2. Ceres Rotational Pole

The arrival of the Dawn spacecraft at Ceres made it possible to substantially improve the accuracy of Ceres's pole position and rotation rate. The present-day obliquity of Ceres is $\approx 4.02^\circ$. For the present study, we used the spin pole location and rotation rate derived from the Dawn measurements. Specifically, the PCK SPICE kernel

Table 1. Summary of the BCFDs

| ID | ϕ (deg) | λ (deg) | BCFD Area (km ²) | Brightness Ratio to Immediate Surrounding | Crater Diameter (km) | Comments |
|----------------------|--------------|-----------------|------------------------------|---|----------------------|---|
| NP4 central part | +86.2 | 79.3 | 2.4 | 3.0 ± 0.8 | 6.5 | Contains a PSR up to $\epsilon = 20^\circ$ |
| NP4 outer part | | | 16.9 | 1.4 ± 0.3 | | |
| NP7 | +77.6 | 353.9 | 0.9 | 1.8 ± 0.3 | 4.6 | Contains a PSR up to at least $\epsilon = 12^\circ$ |
| NP5 shadowed part | +69.9 | 114.0 | 2.4 | 2.7 ± 0.2 | 3.5 | No PSR at DTM resolution. |
| NP5 illuminated part | | | | 2.8 ± 0.2 | | Water ice detected by VIR [Platz et al., 2017] |
| NP26 | +79.0 | 259.1 | 16.0 | – | 8.6 | Contains a PSR up to at least $\epsilon = 20^\circ$ |
| NP19 | +81.3 | 313.9 | 10.8 | – | 6.5 | Contains a PSR up to at least $\epsilon = 12^\circ$ |
| SP1 | –71.3 | 31.2 | 6.9 | 1.6 ± 0.2 | 6.9 | Contains a PSR up to at least $\epsilon = 20^\circ$ |
| SP2 | –69.7 | 168.5 | <1 | – | 2.2 | Not well resolved in DTM |

dawn_ceres_SPC160713.tpc was used for Ceres’s initial orientation. At JD = 2451545.0, the Ceres’s spin pole coordinates are $\alpha = 291.42751^\circ$ and $\delta = 66.76043^\circ$. The uncertainties are on the order of 0.01° .

3.3. Ceres Moments of Inertia

We can constrain the moments of inertia of Ceres using the observed degree-2 gravity field coefficients and a hydrostatic equilibrium assumption. It can be shown (see supporting information) that Ceres’s normalized polar moment of inertia is $C/Mr_{\text{vol}}^2 \approx 0.392$, where $r_{\text{vol}} = 469.7$ km—the radius of a sphere that has a volume equivalent to that of Ceres. Using the relations between moments of inertia and the unnormalized gravity coefficients [Park et al., 2016], we obtain the following:

$$\begin{Bmatrix} A/(Mr_{\text{vol}}^2) \\ B/(Mr_{\text{vol}}^2) \end{Bmatrix} = (C/(Mr_{\text{vol}}^2) - J_2) + \sqrt{C_{22}^2 + S_{22}^2} \cdot \begin{Bmatrix} -2 \\ +2 \end{Bmatrix}, \quad (3)$$

where M is the mass of Ceres; J_2 , C_{22} , and S_{22} are the degree-2 spherical harmonic coefficients of the gravity field; and A , B , and C are the moments of inertia. We used a two-layer model and hydrostatic equilibrium method from Tricarico [2014] to derive moments of inertia from the observed gravity coefficients (see supporting information). The major uncertainty in deriving the moments of inertia is due to nonhydrostaticity of Ceres, which can change C/Mr_{vol}^2 by as much as 0.005 (see supporting information). We therefore chose a range for C/Mr_{vol}^2 between 0.387 and 0.397 for our orbital integrations. For the triaxial Ceres, the equatorial moments of inertia A and B are computed according to equation (3). For the biaxial case, we take the equatorial moment to be $(A + B)/2$. With this choice for the equatorial moment, the precession constant [e.g., Bills and Nimmo, 2011, equation 23] will remain unchanged.

3.4. Bright Crater Floor Deposits

A number of bright crater floor deposits (BCFDs) in PSRs have been identified (Table 1). In general, BCFDs are rare: only 5 out of 49 present-day PSRs larger than 10 km² contain BCFDs. All of the deposits considered for this study lie entirely within the present-day PSRs, except NP5. Light reflected from the high-standing, illuminated crater walls and rims allows identification of the surface features within the shadows. However, this illumination is much weaker than direct sunlight and resolving the surface requires substantial stretching of the image. This inevitably enhances the image noise and artifacts due to image compression. Careful visual inspection of images taken with different illumination geometries and compression ratios is therefore required to recognize real surface brightness variations.

The surface brightness of the BCFDs is 1.4–3.0 times higher than the surrounding area. The brightness of the BCFD in NP5 is 2.8 ± 0.2 higher than its immediate surroundings. However, the entire crater floor of NP5 is brighter than average Ceres. Therefore, if BCFD in NP5 is compared to the shadowed floor of a neighboring crater, it is brighter by a factor of 3.9 ± 0.6 . The facts that NP5 is not entirely in permanent shadow and is much brighter indicate that the nature of this deposit may be different from the others considered in this study. It is important to note that the deposits are seen in diffuse, secondary, illumination. As such we cannot derive the physical or normal albedo, which is defined at a phase angle of zero [Hapke, 1981, 2012].

4. Results

4.1. Obliquity History

We performed a number of orbital integrations with triaxial and biaxial Ceres with different numbers of perturbing planets. Secular dynamics of Ceres is dominated by Jupiter and Saturn modes. As long as Jupiter and Saturn are included and interact with Ceres, we obtain essentially the same obliquity history. The initial positions and velocities of planets were taken from the DE430 ephemeris [Folkner *et al.*, 2014] using the SPICE ancillary information system [Acton, 1996]. We find that the obliquity history is not sensitive to the triaxiality of Ceres. This allows us to use much longer integration time steps since there is no need to resolve Ceres's rotation period, and the triaxial step $B_3(h)$ can be skipped. The results are also not sensitive to relativistic effects, which we modeled as an additional velocity kick.

Currently, the value of the osculating obliquity of Ceres is 4.03° and is on an increasing trend. Ceres's obliquity passed its local minimum 1328 years ago when the obliquity was 2.42° . The most recent obliquity maximum of 18.52° was reached 13,890 years ago (Figure 1a). Our long-term (3 Myr) integrations for triaxial Ceres show that its obliquity undergoes similar large oscillations (Figure 1b). The pattern of oscillations is very regular and with no evidence of chaos. The main period of the oscillation is 24.5 kyr. Obliquity can reach a maximum of 19.6° . The minimum obliquity is 2.0° . Ceres's obliquity distribution is skewed toward the higher values, with a mean obliquity of 12.21° and a median of 13.21° . The obliquity is greater than 15° for more than 40% of the time. The range of obliquity oscillations does not have a strong dependence on the assumed moments of inertia within the limits constrained by the Dawn gravity measurements. We also conducted integrations with a biaxial Ceres for 1 Gyr and obtained analogous results for the amplitude and periodicity of obliquity oscillations. Fortunately, nature has given us a rare opportunity to observe Ceres at a time when polar winters are minimal, which enables more and higher-quality observations of the polar areas.

The obliquity oscillations are driven by the periodic variations in Ceres's orbit inclination which occur with a period of 22 kyr and the pole precession cycles with a period of 210 kyr. Those periods were found by performing a fast Fourier transform to the corresponding orbital angles. The obliquity cycle period is therefore close to the synodic period between the precession period T_p and inclination period T_i . This synodic period is $(T_i T_p) / (T_p - T_i) \approx 24.6$ kyr. The Dawn observations, unlike expected by Bills and Nimmo [2011], show that the obliquity of Ceres is not tidally damped to the lowest energy state. Our results are fully consistent with the recent and independent study of secular obliquity variations by Bills and Scott [2017]. We also find that there is no hemispheric asymmetry in terms of insolation over long timescales (100 kyr and longer); the distribution of the subsolar point latitude at the perihelion is symmetric with respect to the equator. The orbital elements and spin vector orientation time series are provided in the supporting information.

4.2. PSR History

The initial illumination modeling by Schorghofer *et al.* [2016] revealed dozens of craters hosting PSRs. The total area of PSRs is a strong function of the body's obliquity. As expected, the total area in permanent shadow decreases at larger obliquity. Illumination simulations performed over a range of obliquities (2° – 20°) indicate a reduction in PSR area from ≈ 3400 km² at $\epsilon = 2^\circ$ to only ≈ 1.6 km² at $\epsilon = 20^\circ$.

In the northern hemisphere (Figure 2a), we find that only two crater floors remain partly in permanent shadow at $\epsilon = 20^\circ$: NP4 and NP26. The numbering of craters here refers to their entry in a catalog that is yet to be published. Figure 3 shows the shrinking outlines of PSRs as obliquity increases. Among the other identified northern BCFDs, NP7 and NP19 maintain an area of permanent shadow up to $\epsilon = 12^\circ$, while NP5 is likely too small (≈ 3.5 km in diameter) to be resolved by the DTM with confidence.

In the southern hemisphere, we find that part of the floor of crater SP1 remains in permanent shadow at ϵ_{\max} . Although we did not identify other areas in permanent shadow at ϵ_{\max} , due to severe DTM artifacts near the south pole (Figure 2b), it is an intriguing fact that SP1 is the only such example in our results. The other southern bright deposit (SP2) is inside a very small crater (≈ 2.2 km in diameter), below what the DTM can confidently model. Both NP4 and SP1 are 6–7 km craters with steep walls ($\approx 40^\circ$ – 45° slope), the primary reason for the persistence of their shadowed floor at high obliquity.

4.3. Relationship of Persistent PSRs and BCFDs

We find a possible connection between the most persistent PSRs, i.e., regions that stay in permanent shadow at $\epsilon = \epsilon_{\max}$ and BCFDs. Figure 3 shows polar stereographic projections of FC images containing BCFDs and the outlines of PSRs computed using illumination modeling for various ϵ .

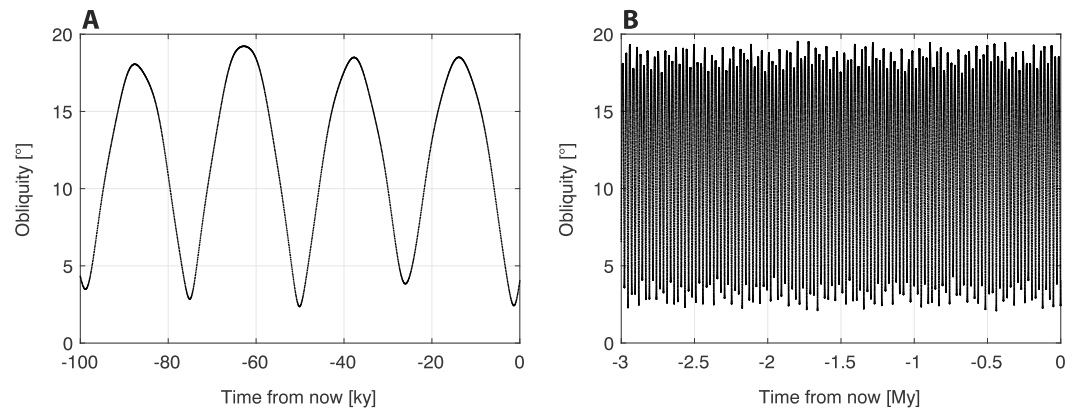


Figure 1. Ceres's obliquity history for $C/Mr_{vol}^2 = 0.392$. (a) Last 100 kyr and (b) last 3 Myr.

4.3.1. NP4

The BCFD in crater NP4 is centered at the location of the most persistent shadows (Figure 3). Interestingly, the NP4 deposit appears to have two brightness gradations of the bottom which are referred to as *central deposit* and the *outer deposit*. The central deposit is two times brighter than the outer one. The outer deposit appears to have a well-defined boundary that approximately coincides with the PSR boundary at an obliquity of 2° .

4.3.2. NP7

The appearance of the BCFD in NP7 (Figure 3) is similar to that in NP4. The NP7 crater remains in shadow up to an obliquity of 12° . However, it is possible that due to the crater's smaller size (4.6 km in diameter), its actual

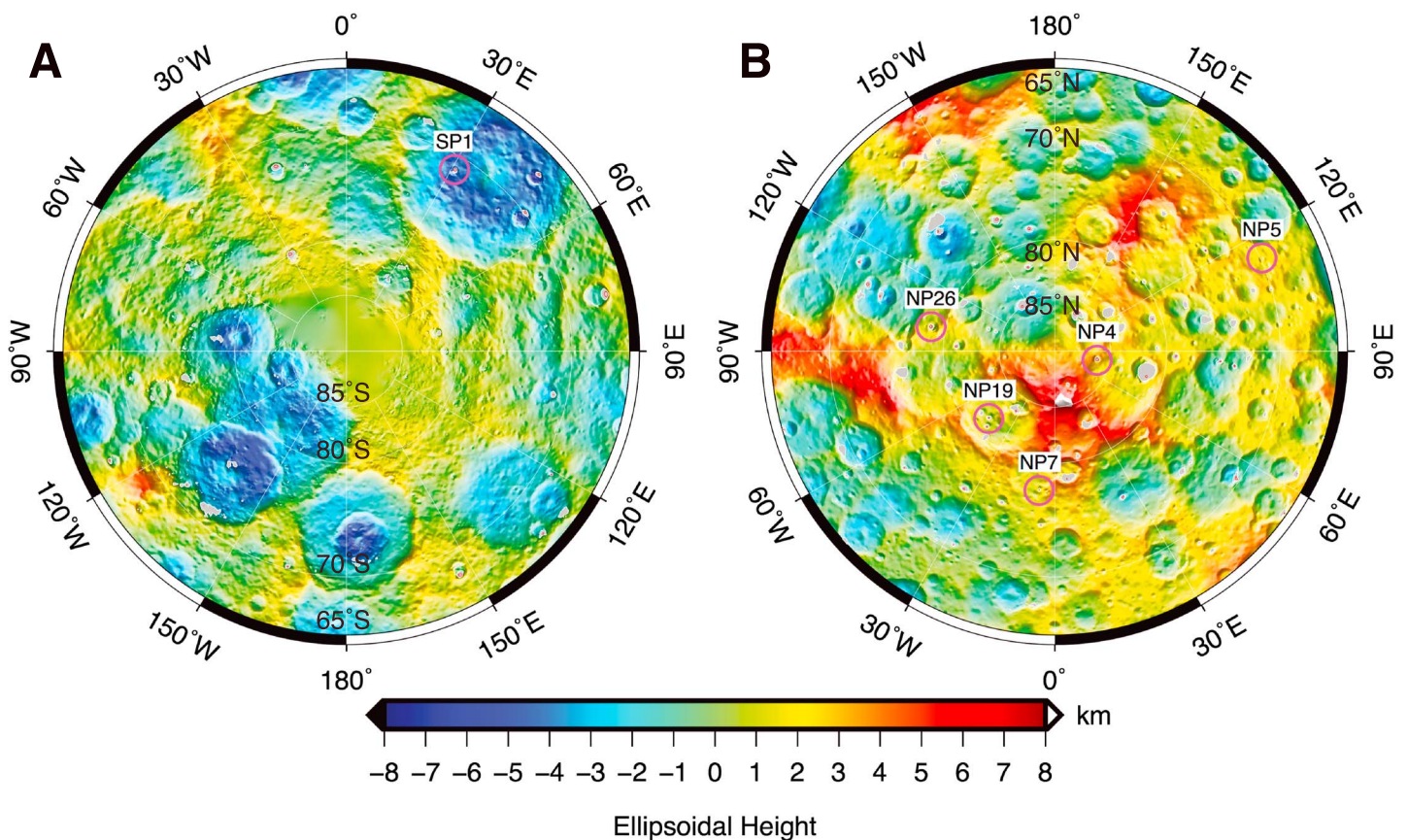


Figure 2. The PSR areas at $\epsilon = 4^\circ$ in the (a) southern and (b) northern hemispheres are shown as filled gray areas. The boundaries for the PSRs at $\epsilon = 12^\circ$ are shown as red contours. The height is with respect to a $482 \text{ km} \times 446 \text{ km}$ ellipsoid.

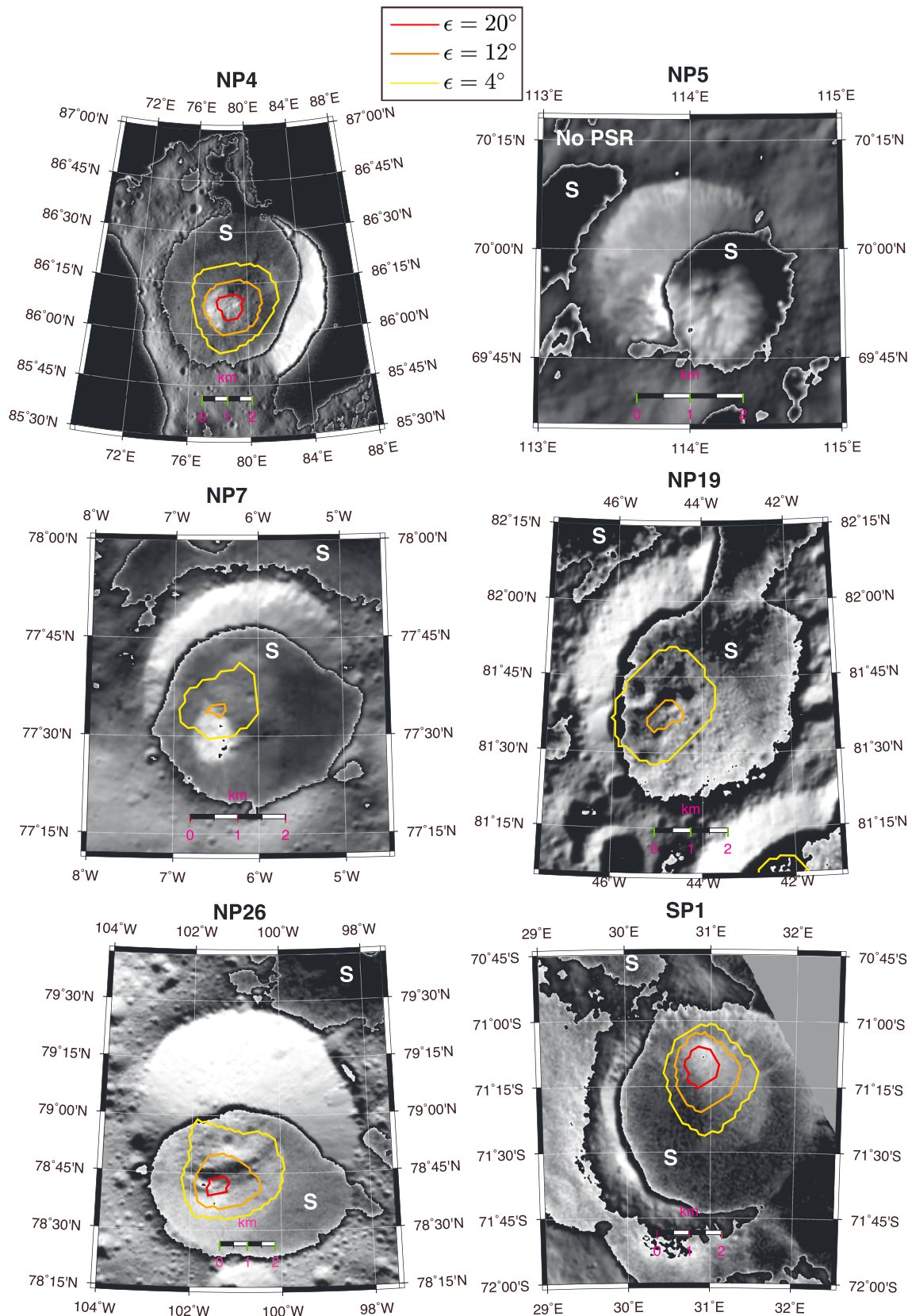


Figure 3. Projected images of BCFDs and the outlines of PSRs for different obliquities ($\epsilon = 4^\circ$, $\epsilon = 12^\circ$, $\epsilon = 20^\circ$). The gray scale of the images is piecewise linear. This is done in order to show both the shadowed and illuminated parts of the surface. The regions in shadow are marked with the letter S.

depth is greater than the depth derived from the HAMO DTM, and thus, it is possible that permanent shadow remains at higher obliquity.

4.3.3. NP5

The NP5 crater is not permanently shadowed at the resolution of the HAMO DTM, but the shadow-stacking method reveals a small PSR [Platz *et al.*, 2017]. The brightness of the BCFD in NP5 is substantially larger than those of the other BCFDs in this study. Part of the BCFD in NP5 extends out of the shadow on FC images (Figure 3) and may be water ice from the measurements of the Visible and Infrared Spectrometer (VIR) instrument [Platz *et al.*, 2017].

A standard one-dimensional thermal model is used to estimate the sublimation rate of an ice deposit at 70° latitude [Schorghofer, 2008]. Assuming a Bond albedo of 0.2 and thermal properties appropriate for bulk ice, the sublimation rate of ice exposed on the surface is $\approx 10^{-3}$ kg m⁻² yr⁻¹ (equivalent to 1 m/kyr). In this case the peak temperature is ≈ 135 K and the mean temperature ≈ 130 K. For lower thermal inertia, appropriate if the ice is not in bulk form, the peak temperature would be higher and the sublimation loss faster. This calculation demonstrates that a sunlit macroscopic ice deposit at this latitude must be geologically young.

4.3.4. NP19

The NP19 crater remains in shadow at an obliquity of 12° (Figure 3). Its bright deposit is qualitatively similar to the one of NP26 and the outer deposit of NP4. We note that the BCFD inside NP19 has the weakest brightness contrast with respect to the surrounding terrain among the deposits considered in this study.

4.3.5. NP26

The NP26 crater remains in shadow up to the maximum obliquity of 20°. Its floor deposit is offset from the crater center and lies partially on the crater wall. The deposit has a sharp and round boundary. There appears to be no morphological difference in the region covered by the bright deposit compared to the surrounding terrain indicating a small thickness of the deposit. The apparent brightness contrast of the deposit in crater NP26 with respect to the surrounding area is lower than for features NP7, NP5, and the central deposit of NP4. Qualitatively, it is similar to the outer deposit in crater NP4 or to the deposit in NP19.

4.3.6. SP1

The SP1 crater is one of the two regions in the southern hemisphere that remains in shadow at an obliquity of 20°. The brightest part of the BCFD corresponds well to the location of the PSR at $\epsilon = 20^\circ$. Further identification of PSRs and BCFDs in the southern polar region will critically depend on the subsequent observing campaign as the subsolar point moves southward.

5. Discussion

Unlike the Moon or Mercury, Ceres's obliquity undergoes rapid and large periodic oscillations. The unique set of bright crater floor deposits in Ceres is correlated with the most persistent of PSRs, i.e., the area that remains in shadow even at the highest obliquity ($\epsilon_{\max} = 19.6^\circ$). In the northern hemisphere, at an obliquity of 20°, only two PSRs remain, both of which host bright deposits. In the southern hemisphere, despite poorer data from Dawn at the time of writing, there remain two PSRs at an obliquity of 20° and one of them has a definite bright deposit. The second most prominent BCFD in the southern hemisphere is located in a 2 km crater that is not well resolved in the HAMO shape model.

Craters NP4, NP19, NP26, and SP1 also possess weaker brightness contrast deposits. Interestingly, the boundaries of those areas approximately correspond to the PSR boundary at the present-day obliquity of 4°. We suggest that this could be due to events of mass wasting that might expose the ground ice. Once the PSR boundary shrinks due to increasing obliquity, these weak deposits are likely to sublimate due to an increased solar incidence flux.

A Monte Carlo model of thermal ballistic hops is used to estimate the fraction of water molecules that will ultimately fall into cold traps. For present-day Ceres this fraction is 0.14% [Schorghofer *et al.*, 2016]. We carried out the same type of Monte Carlo calculation for an obliquity of 10° and a corresponding PSR area of 167 km². We find that the fraction trapped is proportional to the PSR area. Hence, the ratio of fraction trapped to the cumulative PSR area, also known as trapping efficiency, is independent of obliquity. This suggests that permanent shadow over the entire obliquity history is a necessary condition for the formation of the BCFDs, which are likely composed of volatiles deposited via the cold trapping mechanism.

6. Conclusions

We have integrated the obliquity of Ceres over the last 3 Myr for a range of moments of inertia constrained by the Dawn gravity observations. We found that obliquity undergoes large oscillations with a period of 24.5 kyr. Within the range of the Dawn-constrained moments of inertia, our integrations show that obliquity rises to values as high as $\approx 20^\circ$. At such high obliquity, most of the present-day PSRs receive direct sunlight. However, PSRs still exist at an obliquity of 20° . We find a correlation between BCFDs and the most persistent PSRs. In the northern hemisphere, we find that only two PSRs remain at ϵ_{\max} ; these two PSRs contain BCFDs. In the southern hemisphere, we also find that only one crater with a BCFD remains in shadow at ϵ_{\max} . The obliquity excursions offer a simple explanation why most of the present-day PSRs lack BCFDs. The location of BCFDs within persistent PSRs strongly suggests that they consist of volatiles, either water molecules from the exosphere or exposed ground ice.

Acknowledgments

We thank Jack Wisdom for very instructive discussions on symplectic integrators, Javier Roa for helping with implementing relativity, and Matt Siegler and an anonymous reviewer for constructive reviews that helped to improve the manuscript. Part of this research was carried out at the Jet Propulsion Laboratory, California Institute of Technology, under a contract with the National Aeronautics and Space Administration.

References

- Acton, C. H. (1996), Ancillary data services of NASA's navigation and ancillary information facility, *Planet. Space Sci.*, *44*(1), 65–70.
- Arnold, J. R. (1979), Ice in the lunar polar regions, *J. Geophys. Res.*, *84*(B10), 5659–5668.
- Bills, B. G., and F. Nimmo (2011), Forced obliquities and moments of inertia of Ceres and Vesta, *Icarus*, *213*, 496–509.
- Bills, B. G., and B. R. Scott (2017), Secular obliquity variations of Ceres and Pallas, *Icarus*, *284*, 59–69.
- Carry, B., C. Dumas, M. Fulchignoni, W. J. Merline, W. J. Merline, J. Berthier, D. Hestroffer, T. Fusco, and P. Tamblin (2008), Near-infrared mapping and physical properties of the dwarf-planet Ceres, *Astron. Astrophys.*, *478*, 235–244.
- Cavanaugh, J. F., et al. (2007), The Mercury Laser Altimeter instrument for the MESSENGER mission, *Space Sci. Rev.*, *131*, 451–479.
- Chabot, N. L., C. M. Ernst, B. W. Denevi, J. K. Harmon, S. L. Murchie, D. T. Blewett, S. C. Solomon, and E. D. Zhong (2012), Areas of permanent shadow in Mercury's south polar region ascertained by MESSENGER orbital imaging, *Geophys. Res. Lett.*, *39*(9), 1944–8007, doi:10.1029/2012GL051526.
- Chabot, N. L., et al. (2014), Images of surface volatiles in Mercury's polar craters acquired by the MESSENGER spacecraft, *Geology*, *42*(12), 1051–1054.
- Combe, J.-P., et al. (2016), Detection of local H₂O exposed at the surface of Ceres, *Science*, *353*(6303), AAF3010.
- Deutsch, A. N., N. L. Chabot, E. Mazarico, C. M. Ernst, J. W. Head, G. A. Neumann, and S. C. Solomon (2016), Comparison of areas in shadow from imaging and altimetry in the north polar region of Mercury and implications for polar ice deposits, In *Lunar Planet. Sci. Conf.*, *47*, 1134.
- Drummond, J., and J. Christou (2008) Triaxial ellipsoid dimensions and rotational poles of seven asteroids from Lick observatory adaptive optics images, and of Ceres, *Icarus*, *197*(2), 480–496.
- Drummond, J. D., B. Carry, W. J. Merline, C. Dumas, H. Hammel, S. Erard, A. Conrad, P. Tamblin, and C. R. Chapman (2014), Dwarf planet Ceres: Ellipsoid dimensions and rotational pole from Keck and VLT adaptive optics images, *Icarus*, *236*, 28–37.
- Feldman, W. C., S. Maurice, A. B. Binder, B. L. Barraclough, R. C. Elphic, and D. J. Lawrence (1998), Fluxes of fast and epithermal neutrons from Lunar Prospector: Evidence for water ice at the lunar poles, *Science*, *281*(5382), 1496–1500.
- Folkner, W. M., J. G. Williams, D. H. Boggs, R. S. Park, and P. Kuchynka (2014), The planetary and lunar ephemerides DE430 and DE431, *Interplanet. Netw. Prog. Rep.*, *196*, 1–81.
- Hapke, B. (1981), Bidirectional reflectance spectroscopy: 1. Theory, *J. Geophys. Res.*, *86*(B4), 3039–3054.
- Hapke, B. (2012), *Theory of Reflectance and Emittance Spectroscopy*, 472 pp., Cambridge Univ. Press, Cambridge, New York.
- Hayne, P. O., and O. Aharonson (2015), Thermal stability of ice on Ceres with rough topography, *J. Geophys. Res. Planets*, *120*(9), 1567–1584.
- Jakosky, B. M., and R. J. Phillips (2001), Mars' volatile and climate history, *Nature*, *412*(6843), 237–244.
- Jakosky, B. M., R. M. Haberle, and R. E. Arvidson (2005), The changing picture of volatiles and climate on Mars, *Science*, *310*(5753), 1439–1440.
- Laskar, J., A. C. M. Correia, M. Gastineau, F. Joutel, B. Levrard, and P. Robutel (2004), Long term evolution and chaotic diffusion of the insolation quantities of Mars, *Icarus*, *170*(2), 343–364.
- Mazarico, E., G. A. Neumann, D. E. Smith, M. T. Zuber, and M. H. Torrence (2011), Illumination conditions of the lunar polar regions using LOLA topography, *Icarus*, *211*(2), 1066–1081.
- Moores, J. E. (2016), Lunar water migration in the interval between large impacts: Heterogeneous delivery to permanently shadowed regions, fractionation, and diffusive barriers, *J. Geophys. Res. Planets*, *121*(1), 46–60.
- Neumann, G. A., et al. (2013), Bright and dark polar deposits on Mercury: Evidence for surface volatiles, *Science*, *339*(6117), 296–300.
- Paige, D. A., et al. (2010), Diviner lunar radiometer observations of cold traps in the Moon's south polar region, *Science*, *330*(6003), 479–482.
- Park, R. S. et al. (2016), A partially differentiated interior for (1) Ceres deduced from its gravity field and shape, *Nature*, *537*, 515–517.
- Platz, T. et al. (2017), Into darkness: Ice deposits in Ceres' northern permanent shadows, *Nat. Astron.*, *1*, 0007.
- Prettyman, T. H., et al. (2016), Extensive water ice within Ceres' aqueously altered regolith: Evidence from nuclear spectroscopy, *Science*, doi:10.1126/science.aah6765.
- Preusker, F., F. Scholten, K.-D. Matz, T. Roatsch, S. Elgner, R. Jaumann, S. P. Joy, C. A. Polansky, C. A. Raymond, and C. T. Russell (2015), *Shape Model and Rotational State of Dwarf Planet Ceres From Dawn FC Stereo Images*, European Planetary Science Congress, Nantes, France.
- Preusker, F., F. Scholten, K.-D. Matz, S. Elgner, R. Jaumann, T. Roatsch, S. P. Joy, C. A. Polansky, C. A. Raymond, and C. T. Russell (2016), Dawn at Ceres—Shape model and rotational state, in *Proceedings of the 47th Lunar Planetary Science Conference*, vol. 47, pp. 1954, USRA, Houston, Tex.
- Rambaux, N., J. Castillo-Rogez, V. Dehant, and P. Kuchynka (2011), Constraining Ceres' interior from its rotational motion, *Astron. Astrophys.*, *535*, A43.
- Russell, C. T., et al. (2016), Dawn arrives at Ceres: Exploration of a small, volatile-rich world, *Science*, *353*(6303), 1008–1010, doi:10.1126/science.aaf4219.
- Sanin, A. B., et al. (2012), Testing lunar permanently shadowed regions for water ice: LEND results from LRO, *J. Geophys. Res.*, *117*, E00H26, doi:10.1029/2011JE003971.
- Schorghofer, N. (2008), The lifetime of ice on main belt asteroids, *Astrophys. J.*, *682*(1), 697–705.

- Schorghofer, N., E. Mazarico, T. Platz, F. Preusker, S. E. Schroder, C. A. Raymond, and C. T. Russell (2016), The permanently shadowed regions of dwarf planet Ceres, *Geophys. Res. Lett.*, *43*, 6783–6789, doi:10.1002/2016GL069368.
- Schröder, S. E., T. Maue, P. Gutiérrez Marqués, S. Mottola, K. M. Aye, H. Sierks, H. U. Keller, and A. Nathues (2013), In-flight calibration of the Dawn Framing Camera, *Icarus*, *226*(2), 1304–1317.
- Siegler, M. A., B. G. Bills, and D. A. Paige (2011), Effects of orbital evolution on lunar ice stability, *J. Geophys. Res.*, *116*, E03010, doi:10.1029/2010JE003652.
- Siegler, M. A., B. G. Bills, and D. A. Paige (2013), Orbital eccentricity driven temperature variation at Mercury's poles, *J. Geophys. Res. Planets*, *118*(5), 930–937, doi:10.1002/jgre.20070.
- Siegler, M. A., D. A. Paige, J.-P. Williams, and B. G. Bills (2015), Evolution of lunar polar ice stability, *Icarus*, *255*, 78–87.
- Siegler, M. A., R. S. Miller, J. T. Keane, M. Laneuville, D. A. Paige, I. Matsuyama, D. J. Lawrence, A. Crotts, and M. J. Poston (2016), Lunar true polar wander inferred from polar hydrogen, *Nature*, *531*(7595), 480–484.
- Sierks, H., et al. (2011), The Dawn framing camera, *Space Sci. Rev.*, *163*(1–4), 263–327.
- Skoglöv, E., P. Magnusson, and M. Dahlgren (1996), Evolution of the obliquities for ten asteroids, *Planet. Space Sci.*, *44*(10), 1177–1183.
- Slade, M. A., B. J. Butler, and D. O. Muhleman (1992), Mercury radar imaging: Evidence for polar ice, *Science*, *258*, 635–635.
- Snyder, J. R. (1982), Map projections used by the US Geological Survey, *Tech. Rep.*, U.S. Gov. Print. Off.
- Thomas, P. C., J. W. Parker, L. A. McFadden, C. T. Russell, S. A. Stern, M. V. Sykes, and E. F. Young (2005), Differentiation of the asteroid Ceres as revealed by its shape, *Nature*, *437*, 224–226.
- Touma, J., and J. Wisdom (1994), Lie-Poisson integrators for rigid body dynamics in the solar system, *Astron. J.*, *107*, 1189–1202.
- Tricarico, P. (2014), Multi-layer hydrostatic equilibrium of planets and synchronous moons: Theory and application to Ceres and to solar system moons, *Astrophys. J.*, *782*(2), 99.
- Ward, W. R. (1975), Past orientation of the lunar spin axis, *Science*, *189*(4200), 377–379.
- Watson, K., B. C. Murray, and H. Brown (1961), The behavior of volatiles on the lunar surface, *J. Geophys. Res.*, *66*(9), 3033–3045.
- Wisdom, J., and M. Holman (1991), Symplectic maps for the n-body problem, *Astron. J.*, *102*, 1528–1538.
- Zuber, M. T., and D. E. Smith (1997), Topography of the lunar south polar region: Implications for the size and location of permanently shaded areas, *Geophys. Res. Lett.*, *24*(17), 2183–2186.
- Zuber, M. T., et al. (2012), Topography of the Northern Hemisphere of Mercury from MESSENGER laser altimetry, *Science*, *336*(6078), 217–220.